Journal of Zhejiang University-SCIENCE A (Applied Physics & Engineering)
ISSN 1673-565X (Print); ISSN 1862-1775 (Online)
www.jzus.zju.edu.cn; www.springerlink.com
E-mail: jzus@zju.edu.cn

Numerical investigation on wheel-turnout rail dynamic interaction excited by wheel diameter difference in high-speed railway*

Rong CHEN[1,2], Jia-yin CHEN[1,2], Ping WANG[1,2], Jing-mang XU[†‡1,2], Jie-ling XIAO[1,2]

([1]*MOE Key Laboratory of High-speed Railway Engineering, Southwest Jiaotong University, Chengdu 610031, China*)

([2]*School of Civil Engineering, Southwest Jiaotong University, Chengdu 610031, China*)

[†]E-mail: mang080887@163.com

Received Mar. 10, 2017; Revision accepted July 12, 2017; Crosschecked July 27, 2017

Abstract: The wheel-rail relationship in turnout is more complicated than that in ordinary track. Profile wear and machining errors of the wheelset cause deviations of the rolling radius on different wheels. Therefore, wheelsets move to the direction of smaller diameter wheels in search of a new stable state and to change the condition before entering the turnout. The main aim of the present work is to examine the wheel-turnout rail dynamic interaction combined with the static contact behaviour. Calculations are performed on a high-speed vehicle CRH2 and the No. 12 turnout of the passenger dedicated line. The wheel-turnout contact geometric relationship and normal contact behaviour under wheel diameter difference are assessed by the trace principle and finite element method. A high-speed vehicle-turnout coupling dynamic model is established based on SIMPACK software to analyse the wheel-rail dynamic interaction, riding comfort, and wear. Both the wheel diameter amplitudes and distribution patterns are accounted for. The simulation shows that wheel diameter difference can greatly disturb the positions' variation of wheel-rail contact points and affect the normal contact behaviour on switch rails by changing the load transition position. The effect of wheel diameter difference on wheel-turnout rail dynamic interaction can be divided into three according to its amplitude: when the wheel diameter difference is within 0–1.5 mm, the wheel flange comes into contact with the switch rail in advance, causing a rapidly increased lateral wheel-rail force; when it is within 1.5–2.5 mm, trains are subject to instability under equivalent in-phase wheel diameter difference; when it is larger than 2.5 mm, the continuous flange-switch rail contact helps strengthen the vehicle stability, but increases the wheel-rail wear. It is recommended to control the wheel diameter difference to within 2.5 mm but limit it to 2 mm if it is distributed in-phase.

Key words: Wheel diameter difference; Turnout; Wheel-rail contact behaviour; Dynamic performance of wheel-rail system; High-speed railway

http://dx.doi.org/10.1631/jzus.A1700134 **CLC number:** U213.61

1 Introduction

Turnouts (switches and crossings) are essential track equipment that provide flexibility for traffic operation. They are comprised of a switch panel and a crossing panel connected by a closure panel. For the wheels' transfer between rails, the profiles of switch rails and crossing rails are designed to vary along the running direction, causing inherent structural irregularities such as a difference in longitudinal head width and height reduction, resulting in the gradual change of the inclined roll angles of the wheelset (Johansson *et al*., 2011; Wang *et al.*, 2012). As shown in Fig. 1, no transition curve or rail cant is provided in the turnout design, and multiple wheel-rail contacts and the operational wear aggravate the wheel-turnout rail interaction, and this leads to higher maintenance costs than for ordinary parts of the track (Zhang and Luo, 2015).

‡ Corresponding author

* Project supported by the National Natural Science Foundation of China (Nos. 51425804, U1334203, 51608459, and 51378439) and the China Postdoctoral Science Foundation (No. 2016M590898)

ORCID: Rong CHEN, http://orcid.org/0000-0001-8093-6201; Jing-mang XU, http://orcid.org/0000-0003-3240-8652

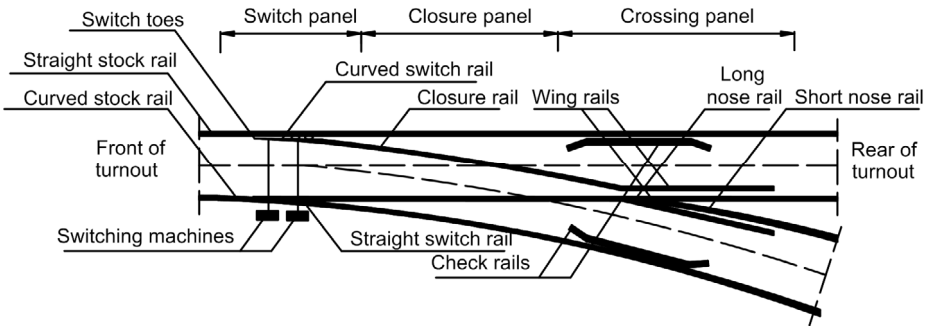

Fig. 1 Schematic plan of turnout with movable nose rails

Another factor affecting the interaction significantly is the wheel profile. The operational wear and machining errors cause the polygon, concave wear, and wheel diameter difference on wheels. The wheel diameter difference refers to the difference of wheels' diameter at both sides of the front or rear wheelset on bogies. Then, the wheelset will move toward the direction of the smaller diameter wheel and change the yaw angle to achieve a new steady state condition, complicating the wheel-rail interaction in the turnout zone. In this paper, the wheel-turnout rail contact behaviour and dynamic characteristics under the excitation of wheel diameter differences are investigated numerically.

Wheel-rail contact characteristics and dynamic interaction at turnout zones have been studied through numerical simulation and field experiments. Based on the wheel-rail contact points' trace principle, a significant factor determining the number of contact points is the elastic penetrations, leading to two-point and multi-point wheel-rail contact methods being put forward. The wheel load transition range was calculated to verify their correctness (Ren *et al*., 2011; Ren, 2013). In addition, the wheel-turnout interaction using different calculation models was widely discussed. The lateral dynamic response of the vehicle-turnout system was analysed for a high-speed train and a normal-speed train passing the No. 12 turnout. In this model, based on the vibration equation of the rail-fastener-sleeper system, seven Euler-Bernoulli beams with uniform sections were used to model the rails in the turnout (Ren *et al*., 2005). A subway vehicle-turnout model was established based on multi-body dynamics software, in which four wheel treads with variation of tread conicities, wear and wheel-rail clearances, two turnout models including the optimized movable nose rail turnout (FAKOP) and typical fixed frog turnout were analysed to characterize the influence of wheel profiles and turnout designs on the vehicle-turnout system (Lagos *et al*., 2012). The simulation results of two dynamic models established by GENSYS and DIFF3D were compared, and the former was applied in a low frequency analysis range (0–20 Hz) while the latter could be used for analysis within a high frequency range. As shown in the comparison result, the dynamic responses coincide with each other given that the rail is a rigid body (Kassa *et al*., 2006). Considering the flexible deformation of the turnout system and having obtained the actual mode of turnout, a finite element model was established and the wheel-rail interaction in turnout zones was analysed using DIFF3D software, which indicated that the wheel-rail force and lateral wheelset displacement are sensitive to the high frequency impact excitation (Kassa and Nielsen, 2009). When compared with the measured data with trains passing three turnouts, the effectiveness of turnout models established by multi-body dynamics and finite elements method was validated (Bruni *et al*., 2009).

All the above studies were based on the nominal turnout section. In order to discuss the effect of turnout profile wear on wheel-rail contact and dynamic performance, a finite element model consisting of measured tram frogs and a worn wheel was used to analyse the contact stress under different axle loads, and this indicated that the slippage of wheels can significantly influence the durability of rails (Kuminek *et al*., 2015). Adopting the von Mises yield criterion for materials and the bilinear kinematic hardening rule (BKIN), a wheel-rail contact finite element model was established to calculate the contact stress and internal stress on turnout rails, showing that profile wear may change the contact stresses by improving the conformal contact and increasing the

surface roughness (Xu *et al.*, 2016). On the other hand, one of the fundamental issues in railway applications is the prediction of wheel and rail profile evolution. Taking the wheel profiles, train speed, wheel-rail friction, and obtained dynamic simulation results as stochastic input parameters, the simplified local 3D contact model was applied and simulation of wear as well as plastic deformation in the rail was achieved with profile smoothing and loop calculation based on the Archard rule (Johansson *et al.*, 2011). Applying the virtual permeation semi-Hertzian method and improved FASTSIM algorithm in the wheel-rail rolling contact model, the non-uniform wear of switch rails was predicted, but it did not consider the plastic deformation of rail material nor wheel wear (Wang *et al.*, 2016).

Based on the research findings in relation to wheel-rail wear, researchers have put forward many methods to study the optimization of wheel profile parameters. The influence of hollow wear wheels on the wheel-rail contact geometric relationship and the running stability was analysed. This indicated that wheel wear causes change of wheel diameter, equivalent conicity as well as nominal rolling radius of wheels at both sides. It reminded us that wheel diameter difference should be considered in the calculations (Sawley *et al.*, 2005). Focusing on the wheel diameter difference, a method was put forward to alleviate the wheel flange wear by adjusting it in the wheelset (Liu *et al*., 2008).

At present, for such key track equipment as high-speed railway turnouts, the above review indicates that some significant research findings have been obtained on the complicated multi-point contact at turnout zones. The effect of wheel-rail wear on the response of vehicle and the dynamic failure of turnout structures has been widely discussed. However, for different distribution of wheel wear at one bogie, there has been little study. As one of the representative factors in wear distribution, the wheel diameter difference in variation of amplitude and distribution patterns is examined in this paper. Having comprehensively analyzed the contact geometric relationship and normal contact behaviour, a high-speed vehicle CRH2 and the Chinese No. 12 turnout on a passenger dedicated line are taken to establish a vehicle-turnout coupling dynamic model based on the rigid multi-body dynamics method. Finally, the dynamic wheel-rail interaction, riding comfort, and wear index of high-speed vehicles running along the straight route of the turnout in facing move (from the switch panel to the crossing panel) are investigated.

2 Motion states of bogies with wheel diameter difference

The wheel diameters at both sides of the wheelset always vary due to operational wear and machining and turning repair errors. The wheel diameter difference refers to the difference in the radius of wheels 70 mm away from the back of wheel. It can be expressed as Eq. (1) in turnout zones:

$$\Delta R = R_{\text{stock}} - R_{\text{switch}}, \tag{1}$$

where R_{stock} and R_{switch} refer to the nominal rolling radius of wheels at the stock rail side and the switch (nose) rail side, respectively. $\Delta R>0$ indicates that the small diameter wheel is at the switch (nose) rail side, and vice versa. As shown in Fig. 2, based on the relationship between the wheel diameter differences of the front and rear wheelsets (ΔR_{front} and ΔR_{rear}) on the same bogie, the wheel diameter difference can be divided into five types that combine in any distribution patterns.

When the small diameter wheel of the guide wheelset is at the left side in forward direction (Fig. 3), the linear speed of the small diameter wheel at the left side is lower than that at the right side under the same rotational angular speed, causing the left wheel to creep forward in relation to the rail with the

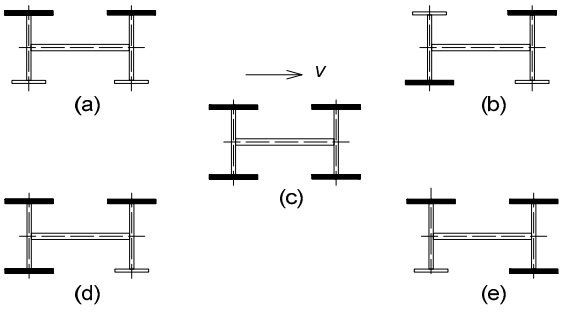

Fig. 2 Wheel diameter difference distribution patterns
The filled wheel is in standard diameter and the blank one is in small diameter. (a) Equivalent in-phase wheel diameter difference ($\Delta R_{\text{front}}=\Delta R_{\text{rear}}\neq 0$); (b) Equivalent anti-phase wheel diameter difference ($\Delta R_{\text{front}}=-\Delta R_{\text{rear}}\neq 0$); (c) Standard wheel diameter ($\Delta R_{\text{front}}=\Delta R_{\text{rear}}=0$); (d) Wheel diameter difference of the front wheelset ($\Delta R_{\text{front}}\neq 0$, $\Delta R_{\text{rear}}=0$); (e) Wheel diameter difference of the rear wheelset ($\Delta R_{\text{front}}=0$, $\Delta R_{\text{rear}}\neq 0$)

traction of the right wheels. Because of the deflecting torque M_{T1} formed by the creep forces T_{Lx1} and T_{Rx1} in the reverse longitudinal direction, the front wheelset is subject to anticlockwise yaw motion. The guide wheelset moves to the direction of the small diameter wheel due to the lateral creep force T_{y1}. The rear wheelset is subject to anticlockwise yaw motion through the transmission of primary suspension forces F_{psRxi}, F_{psLxi}, and F_{psyi} (i=1, 2). Similarly, the rear wheelset is moved laterally to the left under the generated lateral creep force T_{y2}. For the rear wheelset with standard wheel diameter, the distribution of longitudinal creep forces T_{Lx2} and T_{Rx2} and the diameter difference of real rolling circles at both sides are opposite to those of the guide wheelset. The rear wheelset moves to the rail central line under the clockwise deflecting torque and gravity restoring force N_{g2}. Finally, under the action of primary suspension transmission, the front and rear wheelsets do not repeatedly deflect until finding a new equivalent pure rolling line. The wheelset motion can be controlled at equilibrium positions with the help of gravity restoring forces N_{gi} (i=1, 2) or gradually become unstable decided by the type and amplitude of wheel diameter difference.

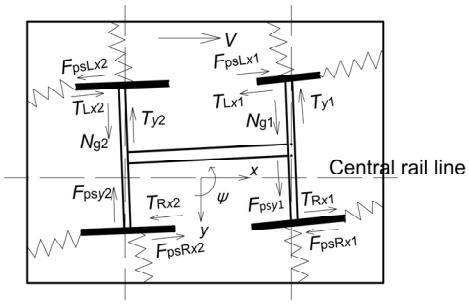

Fig. 3 Motion state analysis of wheel diameter difference of the front wheelset

3 Wheel-rail contact geometric relationship

3.1 Wheel-rail contact points' trace principle

Given wheel diameter differences, we now look at the change of the wheel-rail contact geometric relationship at turnout sections. The wheel-rail profile and wheelset motion state are factors that affect the wheel-rail contact geometric relationship. For wheel-rail contact points' trace principle, since the wheels and rails are considered as rigid bodies and the wheels stay in contact with the rails, the geometric parameters can be considered as a function of the wheelset lateral displacement and yaw angle (Wang, 1984). First, a key turnout section (Fig. 4) is selected for discretization. Then the discrete points obtained are transferred to the global coordinate system from the local coordinate system according to the rail gauge. Curve fitting is performed for the turnout section contour with a cubic spline curve, and a contour curve expressed by a multi-section multinomial is obtained. The discrete points at any turnout section can be expressed based on the linear interpolation made along the longitudinal direction among the discrete points of the key section.

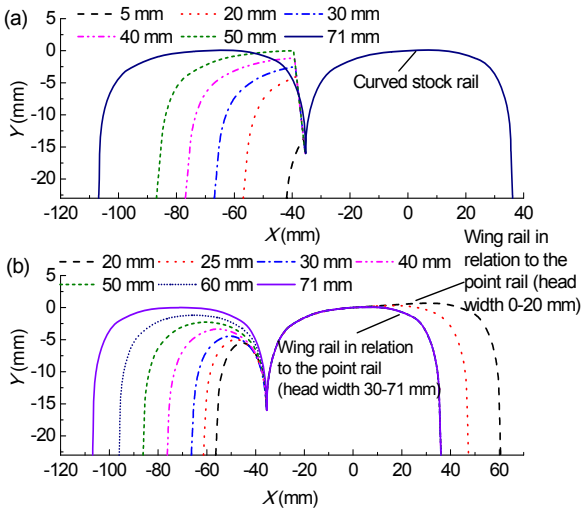

Fig. 4 Key sections of straight switch rail (a) and nose rail (b)

Finally, in the global coordinate system, the wheelsets with wheel diameter differences are moved upward a certain distance. As shown in Fig. 5, the X-axis, Y-axis, and Z-axis represent the center line, transverse direction, and vertical direction of the track, respectively. The O is the point of origin for global coordinate system; C_r and C are the wheel-rail contact point and the lowest point of the rolling circle, respectively; O_c, A, and O_w are the center point of rolling circle, intersection for contact normal and the center line of the wheelset, and the center point of the wheelset, respectively; C'_r, C', O'_c, A', O'_w are the projection points of C_r, C, O_c, A, and O_w, respectively; δ_r and r_r are the wheel-rail contact angle and the radius of rolling circle, respectively; y_w, d_w, ψ_w, and ϕ_w are the lateral displacement of wheelset, the lateral distance between the center point of the wheelset and the center point of the rolling circle, the yaw angle, and the rolling angle of the wheelset, respectively.

According to the spatial geometric relationship, with the changed lateral coordinate value d_w of the rolling circle in the wheelset coordinate system, the contact point C_r is located in three planes, i.e., the plane $AC_rC_r'A'$, the rolling circle plane with center O_c and the spherical surface taking the rolling circle center O_c as its center and r_r as its radius. From Eqs. (2) and (3), the relationship between potential contact points $C_r(x, y, z)$ of different rolling circles and the circle center $O_c(x_{O_c}, y_{O_c}, z_{O_c})$ can be obtained. Therefore, the contact points' trace is combined with a set of potential contact points C_r:

$$\begin{cases} x = x_{O_c} + l_x r_r \tan\delta_r, \\ y = y_{O_c} + y_w - r_r (l_x^2 l_y \tan\delta_r + l_z m)/(1 - l_x^2), \\ z = z_{O_c} - r_r (l_x^2 l_z \tan\delta_r - l_y m)/(1 - l_x^2), \end{cases} \quad (2)$$

$$m = \sqrt{1 - l_x^2 (1 + \tan^2 \delta_r)}, \quad (3)$$

where l_x, l_y, and l_z refer to the cosines of the central wheelset line in the X, Y, and Z directions, respectively.

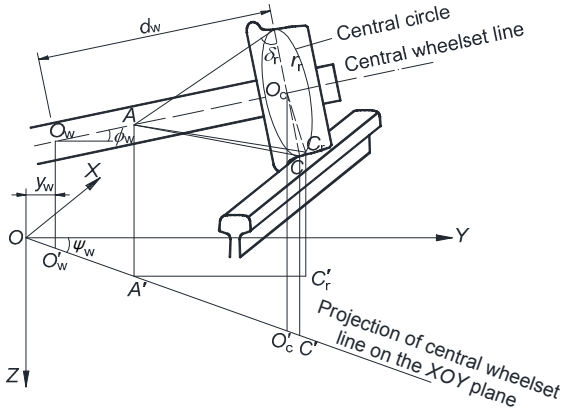

Fig. 5 Wheel-rail contact geometric relationship (taking the right side as an example)

The contact points' trace and rail contours are discretized in the global coordinate system and the vertical distance between wheel-rail discrete points is scanned at both sides. The iteration of the wheelset roll angle is not stopped until the difference of minimum distance between the trace lines and rail contours at both sides satisfies the error that tends to 0. The actual wheel-rail contact points are located at both ends of the minimum vertical distance line.

3.2 Influence of wheel diameter difference on wheel-turnout rail contact geometric relationship

Sections of the switch rail and nose rail at the wheel load transition position are selected in order to study the wheel-rail contact geometric relationship of LMA tread wheels with ±3 mm wheel diameter differences and standard wheel diameter under variable lateral displacements. It can be seen from Table 1 and Fig. 6 that as the wheel diameter difference changes from −3 mm to 3 mm, the range of lateral displacements that the wheel load transits from the stock (wing) rail to the switch (nose) rail gradually diminishes. That is, under the same lateral displacement of wheelsets, the wheel load transition position will be advanced when the small diameter wheel is at the stock rail side. Similarly, the wheel load transition position will be postponed when the small diameter wheel is at the switch rail side.

Table 1 Lateral displacement range for wheel load transferring from stock (wing) rail to switch (nose) rail

Wheel diameter difference (mm)	Lateral displacement range (mm)	
	Switch rail with 35 mm head width	Nose rail with 50 mm head width
−3	−12–−7, 9–12	−12–12
0 (standard wheel diameter)	−12–−7.5, 10–12	−9–0, 5–12
3	−12–−8, 10.5–12	−7.5–−4, 7.5–12

Fig. 7 shows the roll angle change of wheelsets with wheel diameter difference at the wheel load transition positions of the switch rail and nose rail. As the small diameter wheel is at the switch (nose) rail side, the amplitude of the roll angle of the wheelset increases, resulting in a poor riding comfort index.

Fig. 8 (p.666) shows that when the wheelset with a wheel diameter difference within ±6 mm passes the turnout along the track central line, the contact point positions on rails along the longitudinal direction change because of the inherent turnout structure irregularity. When the wheel diameter difference changes from −6 mm to 6 mm, the vertical position of the wheel-rail contact point at the switch panel changes little. As shown in Fig. 8c, when the small diameter wheel is at the stock rail side, since the wheel-rail contact point is outside the rail head of the wing rail before the load transition, the obvious height difference is caused when the contact point transits to the nose rail from the wing rail, leading to the

maximum amplitude of the variation of wheel-rail contact points in vertical position increasing by 16% compared with that with the standard wheel diameter. When the small diameter wheel is at the switch rail side, Figs. 8b and 8d indicate that the lateral positions of the wheel-rail contact points change greatly behind the load transition positions at the switch panel and in front of the load transition positions at the crossing panel, resulting in an obvious change of the wheel-rail contact angle.

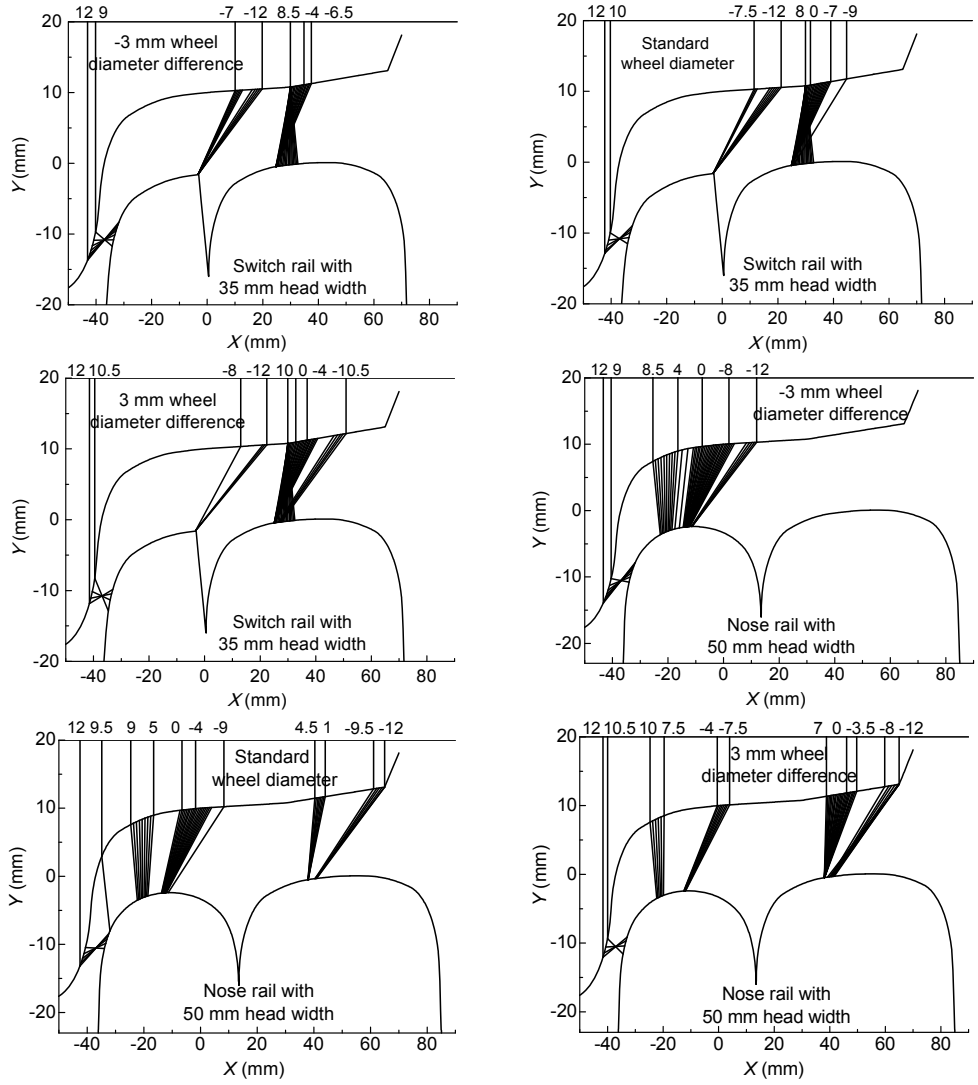

Fig. 6 Distribution of contact points

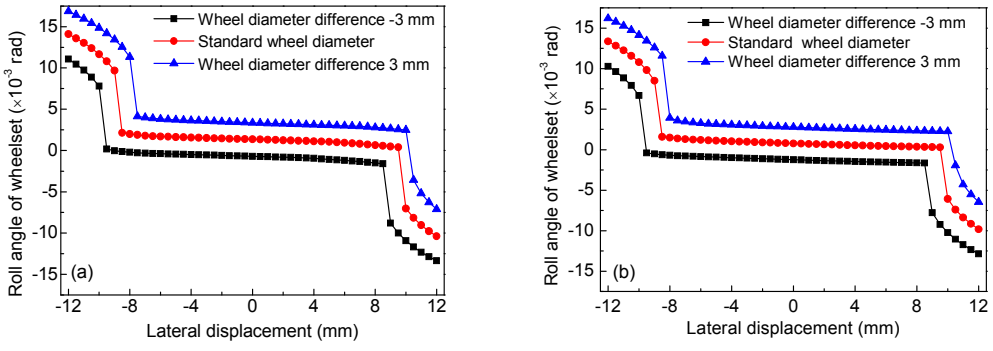

Fig. 7 Roll angle of wheelset: (a) switch rail with 35 mm head width; (b) nose rail with 50 mm head width

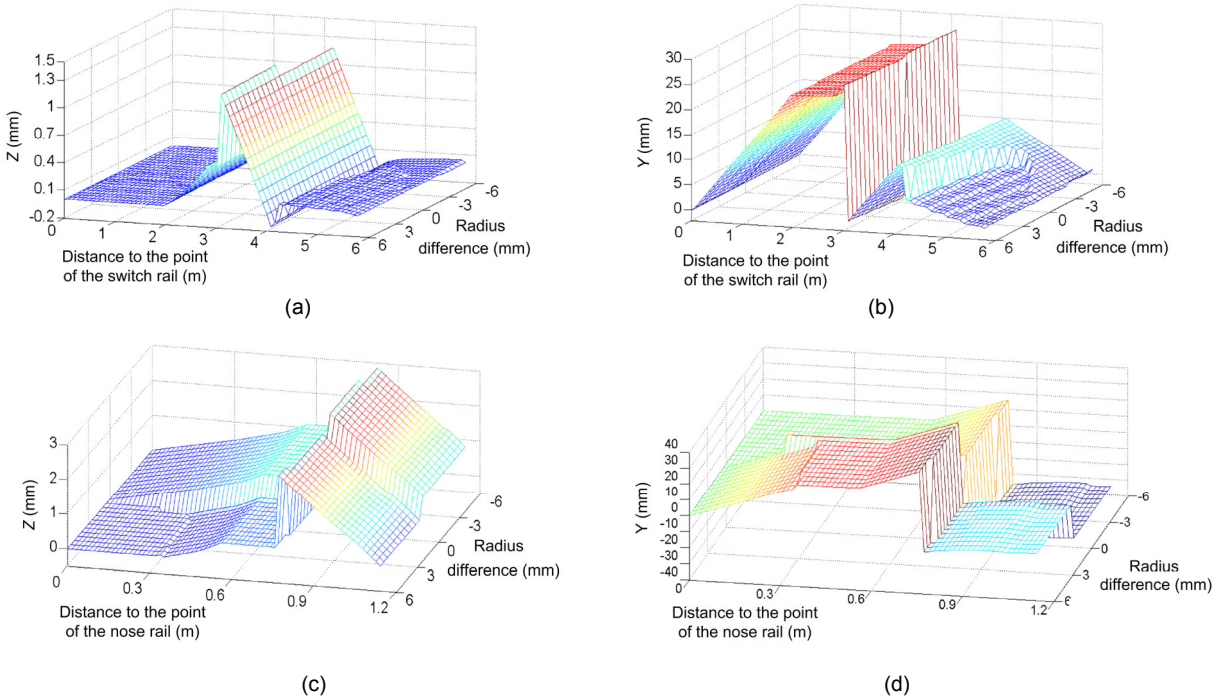

Fig. 8 Variation of wheel-rail contact point positions along the longitudinal direction: (a) vertical position of switch panel; (b) lateral position of switch panel; (c) vertical position of crossing panel; (d) lateral position of crossing panel

4 Contact patch and contact pressure

4.1 Calculation model

The wheel-rail contact in the turnout area is more complicated than that in the interval line as the multi-point contact occurs. When the wheel flange slides along the working edge of rails and the wheel tread contacts the point of the switch rail, a large stress concentration is found. Therefore, the material plastic property should be considered and the finite element method is used to deal with the contact behaviour.

The ANSYS software is applied to simulate the wheel-turnout rail contact (Fig. 9). First, the wheelset model is built to take the wheelset roll angle caused by wheel diameter difference into account. Moreover, the rail cross-section in the switch rail panel at the rail head width of 40 mm near the load transition position is selected to build the turnout model. Then, the vertical displacements of wheelset elements are allowed to take place and the ends of rails at two adjacent fastener systems are constrained in all directions. The wheel and rail bodies are treated as flexibilities and divided into a number of elements. The surface element sizes meshed around the contact region are as small as 1 mm, while those far away from the contact elements are as large as 6 mm. Finally, the axle load is applied at the primary suspension position of the wheelset to deal with the static analysis. The bilinear kinematic hardening material model is applied to describe the elastic-plastic property of materials. This model obeys the bilinear kinematic hardening rule and von Mises yield criteria that can be expressed as follows:

$$\sigma_{\mathrm{e}}=\frac{1}{\sqrt{2}}\sqrt{(\sigma_1-\sigma_2)^2+(\sigma_2-\sigma_3)^2+(\sigma_3-\sigma_1)^2}\geq\sigma_{\mathrm{s}}, \tag{4}$$

$$\sigma=\begin{cases}E_{\mathrm{e}}\varepsilon, & \varepsilon\leq\varepsilon_{\mathrm{s}},\\ \sigma_{\mathrm{s}}+E_{\mathrm{p}}(\varepsilon-\varepsilon_{\mathrm{s}}), & \varepsilon>\varepsilon_{\mathrm{s}},\end{cases} \tag{5}$$

where σ and ε are the stress and strain of rails, respectively; σ_{e} is the equivalent stress; σ_1, σ_2, and σ_3 are the principal stresses; σ_{s} and ε_{s} indicate the stress and strain at the yield point, respectively; E_{e} and E_{p} are the Young's modulus and the strain hardening modulus,

respectively with E_e=210 GPa and E_p=14.897 GPa. As the equivalent stress σ_e satisfies Eq. (4), the material comes into the plastic deformation state.

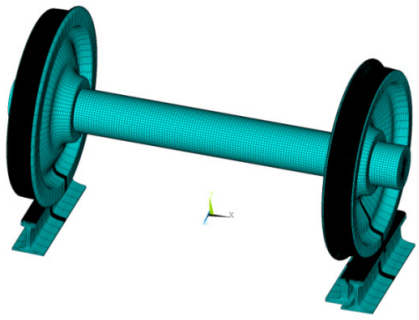

Fig. 9 Wheel-turnout rail contact finite element model

4.2 Calculation

The curved stock rail bends outward with the gradually increased top width of the switch rail. Normally, the wheelset offset to the switch rail side is found when trains pass the turnout in facing move. As the kinematic analysis mentions above, the wheel moves laterally in the direction of the small diameter wheel. Therefore, different wheelset offset positions of 0–9 mm in the direction of the switch rail side corresponding to the positive wheel diameter difference 0–3 mm are selected to compare the simulation results, which are shown in Fig. 10.

It suggests that the contact patches area on the switch rail surface is reduced while that on the curved stock rail surface is enlarged with increased wheel diameter difference. When the wheelset offset is within 3 mm, both the switch rail and curved stock rail bear the load together and the change of the contact pressure on the switch rail is opposite to that on the curved stock rail, leading to the peak value on the switch rail as the wheel diameter difference reaches 2 mm. When the wheelset offset is 6 mm, the two-point contact and stress concentration phenomenon at the point of the switch rail gradually disappear causing the contact pressure on the curved stock rail to increase. However, the wheel diameter difference does not always increase the contact pressure. As shown in the wheelset offset position of 9 mm, the high wheel diameter difference optimizes the contact position on wheel and rail surface. This decreases the contact pressure compared with the nominal wheelset. In addition, the quite different change of contact distribution in the switch rail affects that on straight stock rail side. When the wheelset offset is 0 mm, with the added wheel diameter difference, the radius of curvature at the contact point on the wheel tread transfers from infinity to 450 mm, which improves the conformal contact and decreases the contact stresses. Similarly, as the wheelset moves transversely, no significant change of contact pressure on straight stock rail is found as the radius of curvature at the contact point changes little.

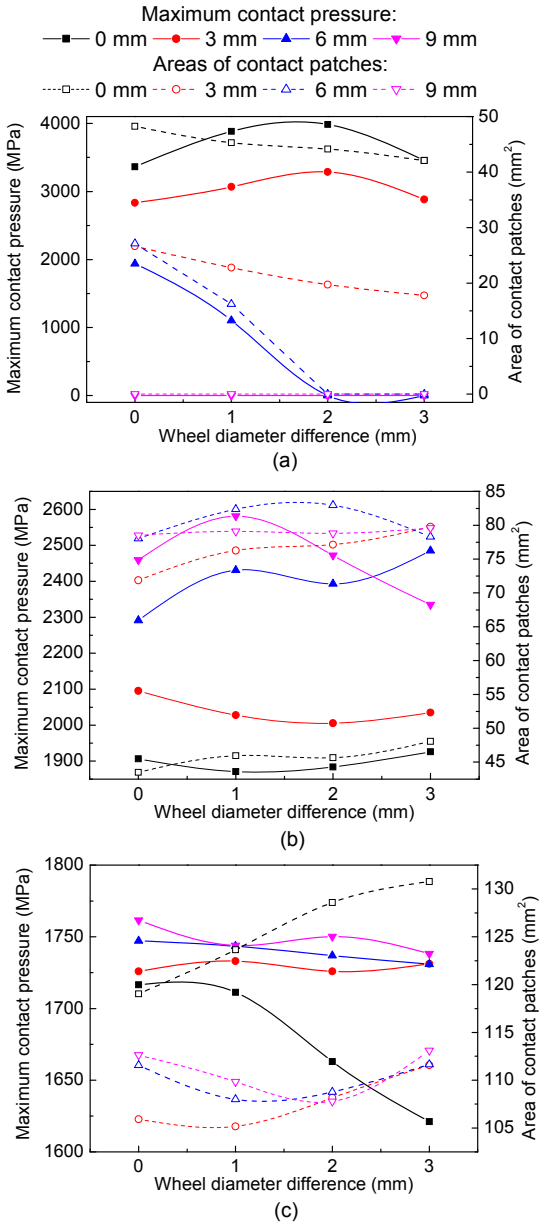

Fig. 10 Maximum contact pressures and areas of contact patches at various wheelset offset positions: (a) switch rail; (b) curved stock rail; (c) straight stock rail

5 Dynamic performance of wheel-rail system at high-speed turnout zones

5.1 Calculation model

In this section, taking the Chinese CRH2 high-speed railway vehicle as the prototype, the validated multi-body dynamics commercial software SIMPACK was adopted to establish the vehicle-turnout coupling dynamics model that has three parts, i.e., vehicle, turnout, and wheel-rail contact (Ling *et al*., 2014). Fig. 11 shows the establishment process of the vehicle model from the substructure to the main structure, including the wheelset, bogie, and car body, all assumed to be rigid bodies. The six DOFs, namely longitudinal movement, lateral movement, vertical movement, roll, pitch, and yaw are considered for seven rigid bodies, comprising 42 DOFs in total (Han *et al*., 2015). Springs and damping elements are used to simulate the secondary force elements between the car body and the two bogies as well as the primary force elements between the two bogies and four wheelsets. The parameter values of the vehicle model are given in (Xu *et al*., 2016). The force elements and joint patterns of the model are marked on the topological graph.

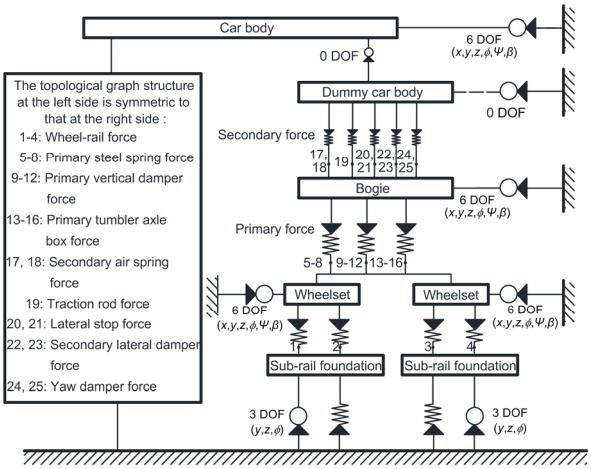

Fig. 11 Topological graph of vehicle model

The simulated turnout model is based on the Chinese No. 12 turnout with a movable nose rail of the passenger dedicated line. The varied rail profiles are realized by sampling the nominal cross-sections of switch rails and nose rails at certain longitudinal positions. Having performed linear interpolation between discrete points of adjacent sampling sections, cross-sections could be obtained with 1 mm intervals of the head width. This ensures the linear variation of the head width and height reduction value for the switch rail and nose rail. Finally, taking the arranged turnout sections according to mileage as inputs, the variable profiles of the turnout are interpolated by means of Bézier curves along the longitudinal direction.

The accuracy of the calculation is determined by the fitting precision of turnout profiles and the simulation of turnout structure. However, there is always a trade-off between accuracy and computational efficiency in dynamic simulation. To highlight the superiority of computational efficiency for multi-body dynamics, the rails are simulated with massless elements and simplified to be fixed on sleeper and ballast, which ignores the characteristics of the fastener system. Then, the sub-rail foundational elements, including the sleeper and ballast, are simulated with a rigid mass together of three DOFs, namely lateral movement, vertical movement, and roll (Fig. 12). The spring-damping elements with stiffness K_y, K_z, K_ϕ and damping C_y, C_z, C_ϕ in the lateral, vertical, and rolling directions are used to create the transitions from subgrade to sub-rail foundation. Finally, joints are set to ensure that the foundations follow the track at the position of the wheelset.

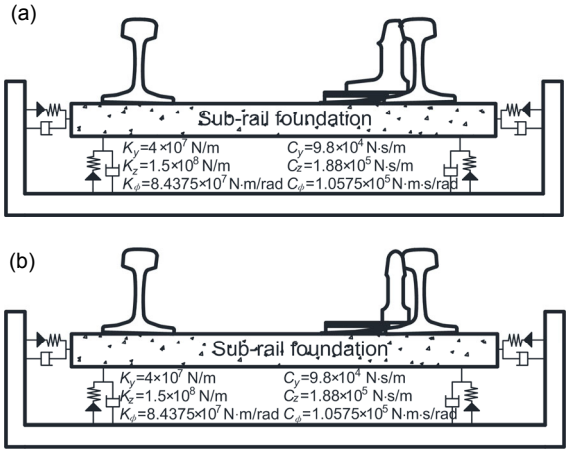

Fig. 12 Turnout model sections in switch panel (a) and crossing panel (b)

The wheel-rail contact serves as a link for the interaction between the dynamic model of the vehicle and the high-speed turnout. The model includes the identification of the contact patch and solution of the normal and tangential contact forces. The number and location of contact patches are determined through calculating the elastic wheel-rail interpenetrations in

the *YOZ* plane. The equivalent elastic contact algorithm converts the contact patches into equivalent ellipses coinciding with their areas and generated wheel-rail contact forces. The normal contact force is determined based on the Hertz nonlinear contact method by calculating the normal wheel-rail elastic penetration. The improved FASTSIM algorithm is adopted to determine the tangential wheel-rail contact force. The calculated wheel-rail contact force can be distributed vertically and laterally in the whole system through the wheel-rail contact angles, reflecting the coupling interaction between the vehicle and turnout systems.

As the wheel-turnout rail impact is more significant at higher velocity, it is of interest to apply the allowed passing speed of 200 km/h on a straight route in the simulation. It is assumed that bogies are subject to equivalent in-phase and anti-phase wheel diameter differences within the amplitude range of 0–4 mm, and that the small diameter wheel of the guide wheelset locates either at the stock rail side or the switch rail side. The dynamic wheel-rail interaction, riding comfort, and wear index at the turnout zones are analyzed comprehensively.

5.2 Dynamic wheel-rail interaction

As trains pass the nose rail and switch rail, peak values of vertical and lateral wheel-rail forces in Fig. 13 are found, and these indicate that the wheel diameter difference has a close relationship to the dynamic characteristics of the system. When the wheel diameter difference is subject to equivalent in-phase distribution, Fig. 14a shows that as the wheel diameter difference changes from −4 mm to 4 mm, the lateral displacement of the guide wheelset changes according to the positions of small diameter

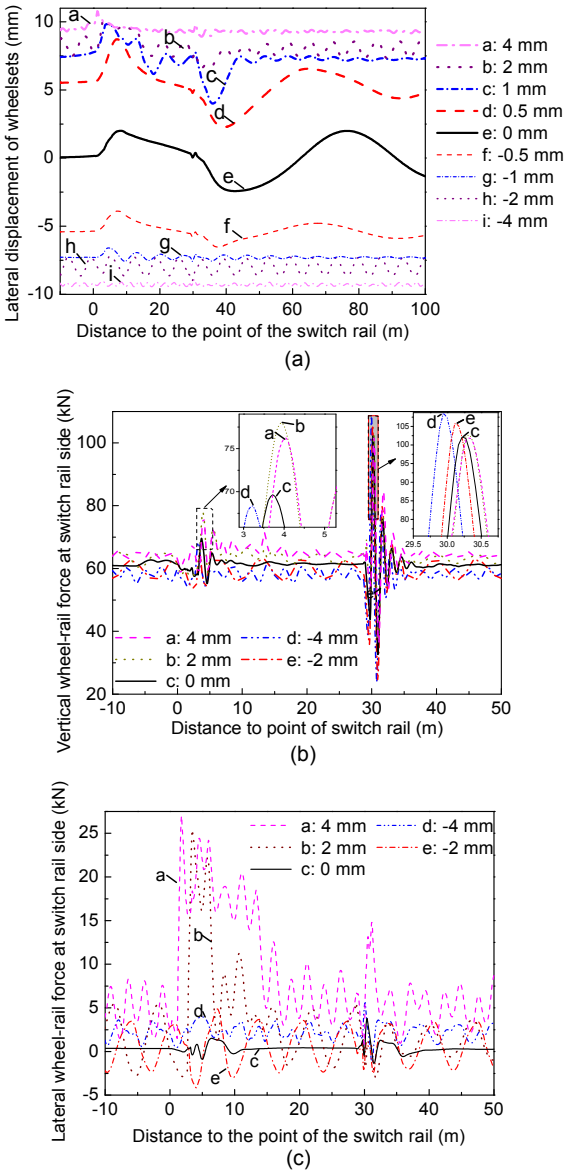

Fig. 14 Dynamic interaction of equivalent in-phase wheel diameter difference: (a) lateral displacement of wheelset; (b) vertical wheel-rail force; (c) lateral wheel-rail force

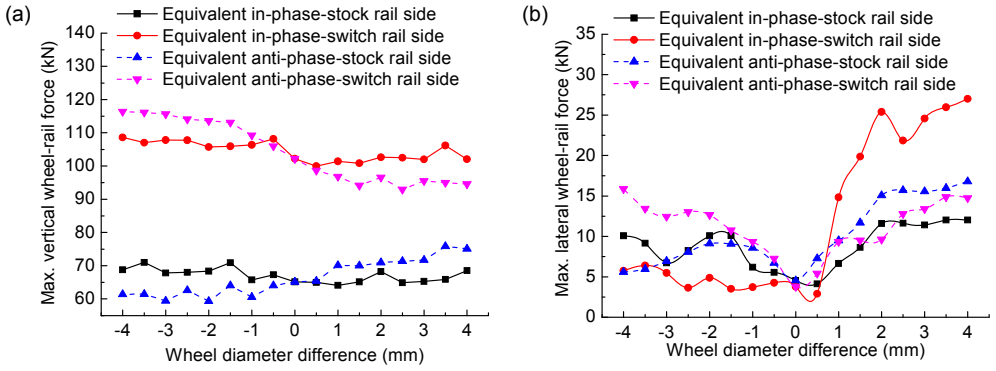

Fig. 13 Maximum wheel-rail force: (a) vertical wheel-rail force; (b) lateral wheel-rail force

wheels. As shown in Fig. 14b, the vertical wheel-rail force at the switch panel increases and that at the crossing panel is similar to that obtained with a standard wheel diameter. The maximum vertical force is independent of the wheel diameter difference.

As shown in Figs. 13b and 14c, when the small diameter wheel is at the switch rail side and the wheel diameter difference is within 1.5 mm, the lateral wheel-rail force increases rapidly, and the lateral displacement of the wheelset is greatly affected by the impact in the switch rail. When the wheel diameter difference is 2 mm, the lateral wheel-rail force at the switch rail side reaches 25.40 kN, which is 5.7 times larger than that obtained under standard operating conditions, and the train is subject to long wavelength hunting motion. When the wheel diameter difference is 3−4 mm, the lateral wheel-rail force gradually stabilizes. On the other hand, as the small diameter wheel locates in the stock rail side, the wheelset moves towards the stock rail side laterally with increased amplitude of wheel diameter difference, reducing the wheel-turnout interaction. The lateral wheel-rail force at the switch rail side is independent of the wheel diameter difference, while that at the stock rail side increases when the wheel diameter difference is within 0–1.5 mm. The peak value is 10.40 kN, 1.25 times larger than that obtained under standard operating conditions. It stabilizes when the wheel diameter difference is larger than 1.5 mm.

In order to characterize the influence of equivalent in-phase wheel diameter difference on the dynamic wheel-rail interaction, Fig. 15 shows the multi-point wheel-rail contact distribution. The contact points of the standard diameter wheel are always near the nominal rolling circle. Tread contact points transit to the switch rail with width 40 mm from the stock rail and transit to the long nose rail with width 48 mm from the wing rail. The wheel-rail force clearly changes within a short frog transition range.

The wheelset moves laterally to the switch rail as the wheel diameter difference increases, and the contact point on the wheel tread moves toward the flanges. When the wheel diameter difference is 1 mm, the contact area between the flanges and switch rail enlarges after the wheel load transition on the switch rail. The generated lateral wheel-rail force and load transition response superpose, and the contact point is restored to a single-point tread contact as the wheel reaches the switch rail with 71 mm head width. When the wheel diameter difference is 2 mm, the vehicles are subject to long wavelength hunting motion. Flange contact of the wheels occurs where the head width of the switch rail is 34 mm, affecting those sections with smaller head width and weaker structures. The lateral wheel-rail force on the flange increases and is subject to sudden positive superposition together with the subsequent lateral force caused by wheel load transition. One-point tread contact is restored at the turnout closure panel. When the wheel diameter difference increases to 3 mm, the advanced flange contact continuously increases the lateral force. The large lateral displacement makes the flanges come close to the working edges of the rail. The equivalent conicity and contact angle at the flange change greatly under low lateral displacement. It is easy for the wheelset to reach the dynamic equilibrium points, making the lateral displacement amplitude close to 0 and a preferable stability. Similarly, as the wheel diameter difference increases to 4 mm, the main contact point wobbles laterally at a low amplitude and high frequency near the flange. The rolling circle diameter and contact angle change quickly with short lateral displacement, causing the lateral wheel-rail force to reach 27.01 kN at the switch rail. To sum up, the lateral wheel-rail force is controlled by the combination of flange-switch rail contact and the stability of the vehicle.

When the small diameter wheel is at the stock rail side, the wheelset moves towards the stock rail side and the flange at the switch rail side does not impact the switch rail again. The lateral wheel-rail force at the switch rail side relies on the wheel load transition, so the simulation results are similar to those at a standard wheel diameter.

Added wheel diameter difference subjected to anti-phase distribution leads to lateral offset of the front and rear wheelset in the opposite direction. This enlarges the yaw angle of the bogie and causes uneven distribution of the vertical wheel-rail forces at both sides. As shown in Fig. 13a and Fig. 16b (p.672), when the wheel diameter difference changes from −4 mm to 4 mm, the vertical wheel-rail force at the switch rail side decreases, while that at the stock rail increases. The difference of the vertical wheel-rail force for wheels at both sides is dependent on the position of the small diameter wheel of the guide

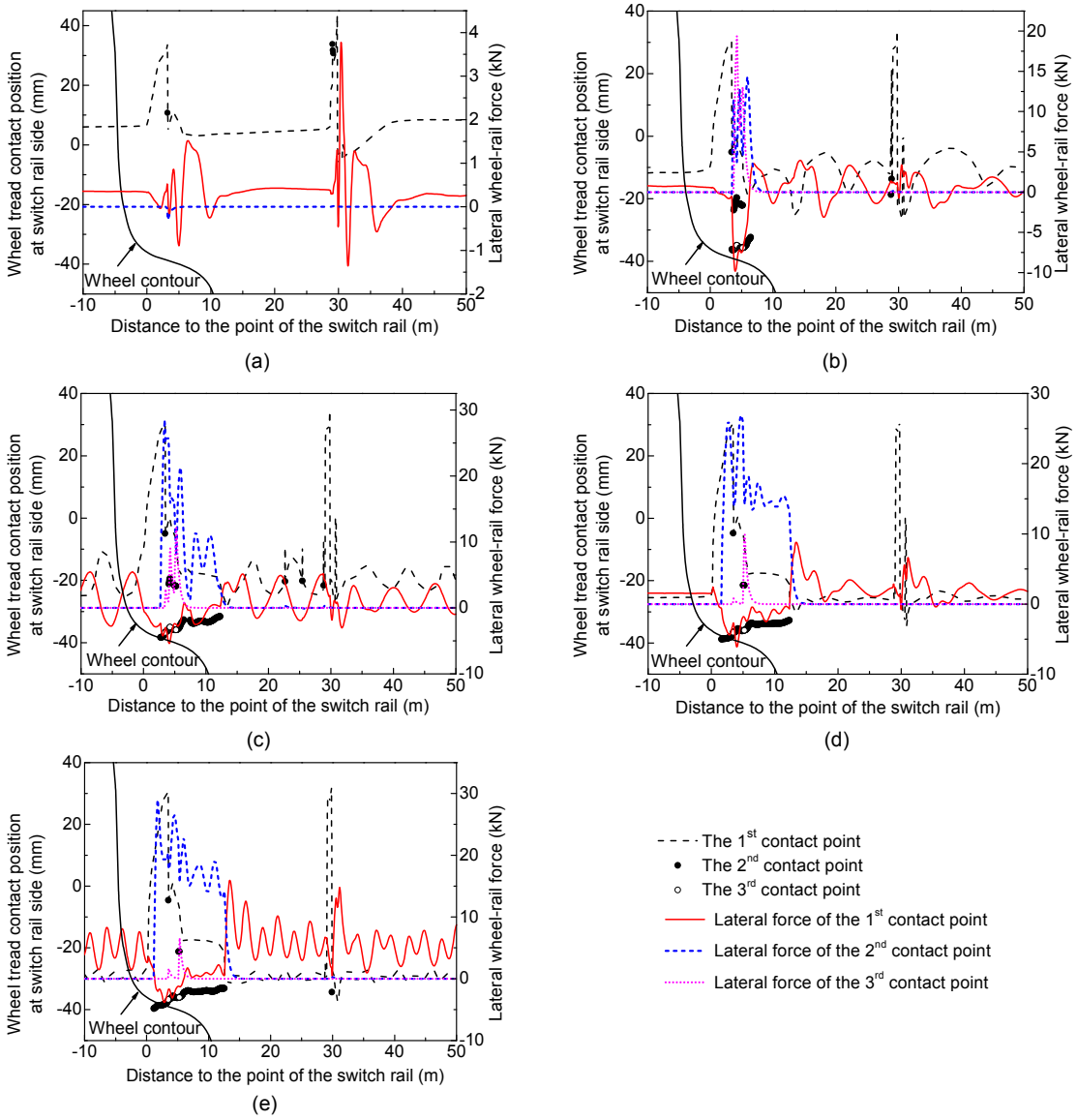

Fig. 15 Lateral positions of contact points on wheel at the switch rail side in variation of equivalent in-phase wheel diameter difference: (a) 0 mm; (b) 1 mm; (c) 2 mm; (d) 3 mm; (e) 4 mm

wheelset and reaches the peak value as the wheel diameter difference reaches −4 mm. The vertical force at the nose rail side can reach 116.39 kN, an increase of 14.18 kN compared with that obtained under standard operating conditions.

As shown in Fig. 16c and Fig. 17 (p.673), when the small diameter wheel of the guide wheelset is at the switch rail side, the flange contact position advances as the wheel diameter difference increases, and the scope of multi-point contact is enlarged near the load transition position. The lateral force direction at the main contact point is opposite to that at the flange contact point. Considering the restriction caused by the reverse yaw angles of the front and rear wheelsets, though the wheel diameter difference amplitude is large, the composite moment on the wheelset is liable to balance on pure rolling lines, so the superposed lateral force is lower than that of the in-phase equivalent.

When the small diameter wheel is at the stock rail side, the guide wheelset moves laterally towards the stock rail side, and the direction of the lateral force at the main contact point is the same as that of the wheel load transition impact. Their positive superposition also causes high lateral wheel-rail force,

indicating that the positions of small diameter wheels do not influence the lateral force amplitude much. When the wheel diameter difference is −4 mm, the maximum lateral force at the switch rail side reaches 15.87 kN, 3.2 times higher than that obtained under standard wheel diameter conditions.

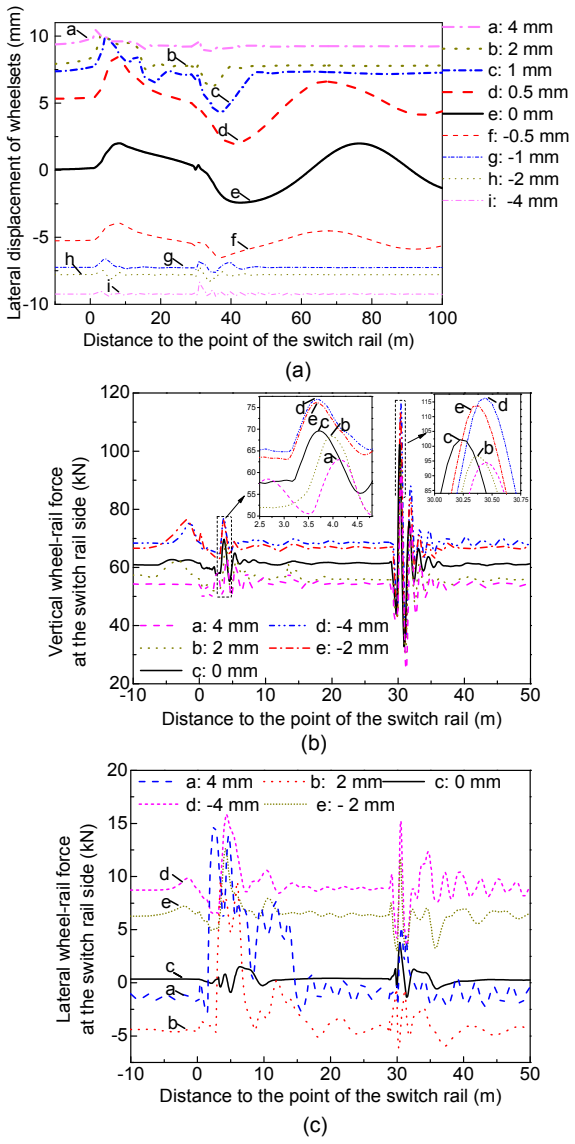

Fig. 16 Dynamic interaction of equivalent anti-phase wheel diameter difference: (a) lateral displacement of wheelset; (b) vertical wheel-rail force; (c) lateral wheel-rail force

5.3 Evaluation of riding comfort

The hunting motion with shallow wave depth and long wavelength along the central rail line is found after trains pass through turnouts. As a result, the Sperling indices are adopted to evaluate the effects of wheel diameter difference on riding comfort in vertical and lateral directions. This can be expressed by

$$W = 7.08[A^3 F(f)/f]^{0.1}, \tag{6}$$

where W refers to the Sperling index; A is the acceleration of trains vibration (g); f indicates the vibration frequency (Hz) and $F(f)$ points to the frequency correction coefficient (NBS, 1985). The Sperling index should be below 2.5 for high-speed electric multiple units (MOR, 2008).

As shown in Fig. 18, when the wheel diameter difference amplitude is within 0.5–1 mm, the dynamic response of trains caused by the impact of various rail profiles increases. However, after trains pass turnouts, the wheelset moves laterally to the equivalent pure rolling line that is offset from the track central line. The wave depth of hunting motions of wheelsets is reduced, causing less change of the Sperling index. Then, when the wheel diameter difference is subject to in-phase distribution and the amplitude reaches 2 mm, unstable hunting motion with long wavelength occurs, which leads to poor riding comfort. The Sperling index reaches 2.23, a 94% increase on that obtained under standard wheel diameter conditions. This is close to the specification limit. When the wheel diameter difference reaches 3 mm, the large lateral displacement causes the wheel flanges to contact constantly with the rail edge at the switch panel. The wheelset reaches the dynamic equilibrium point quickly after the turnout impact. Then the Sperling index decreases and gradually stabilizes.

When the wheel diameter difference is subject to anti-phase distribution, the tendency of reverse yaw motion of the front and rear wheelsets help enhance the stability of bogies to avoid the hunting motion. With the wheel diameter difference changes from −4 mm to 2 mm, the yaw angle of the guide wheelset changes from negative to positive. The impact between the wheelset and switch rail strengthens the lateral dynamic response, causing the Sperling index to reach 1.55 and thus offer poorer riding comfort. When the wheel diameter difference is over 2 mm, the high lateral displacement towards the switch rail side keeps the flange contacting the rail edge, so the Sperling index is reduced and gradually stabilized.

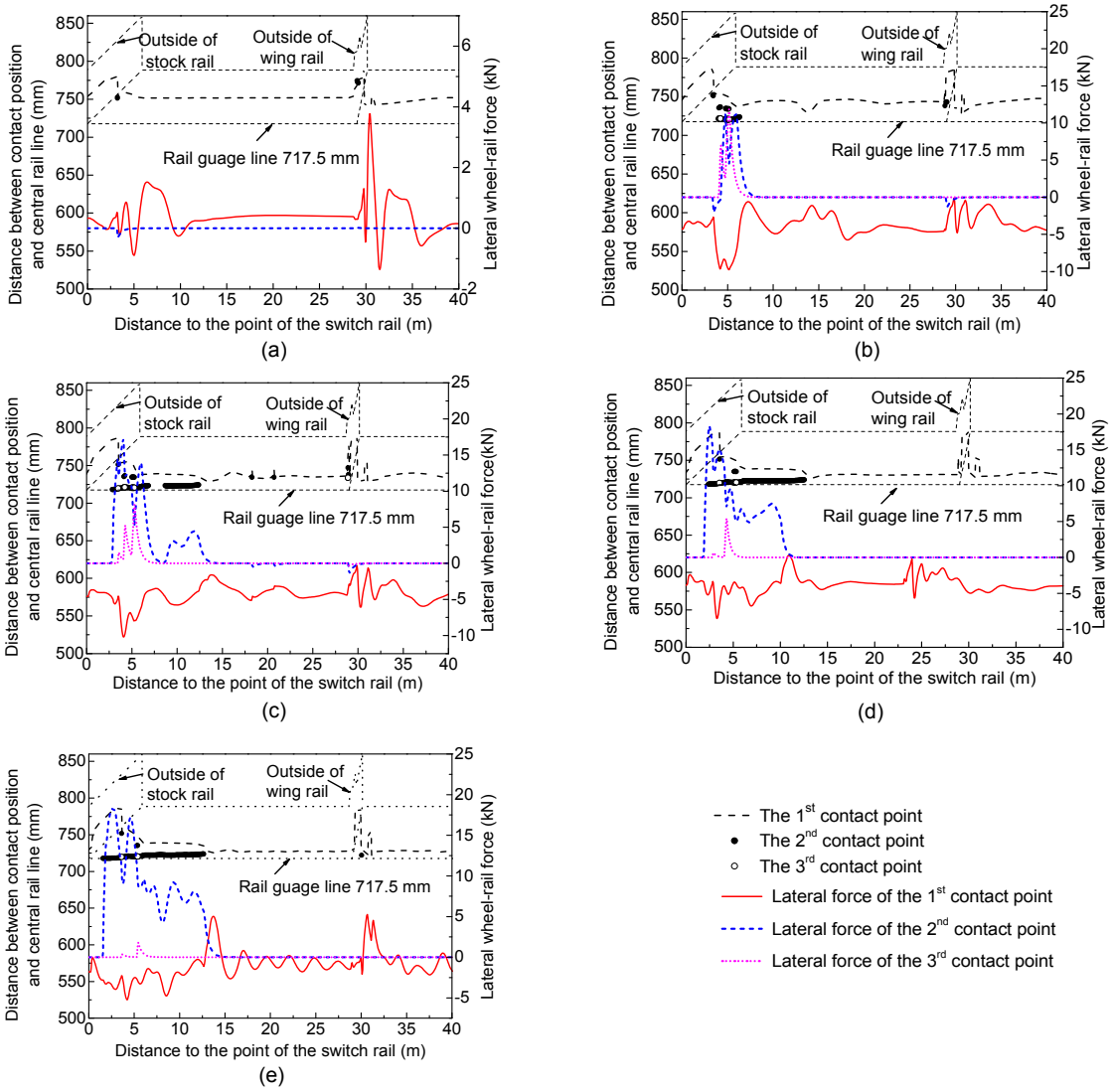

Fig. 17 Lateral positions of contact points on switch rails and nose rails in variation of equivalent anti-phase wheel diameter difference: (a) 0 mm; (b) 1 mm; (c) 2 mm; (d) 3 mm; (e) 4 mm

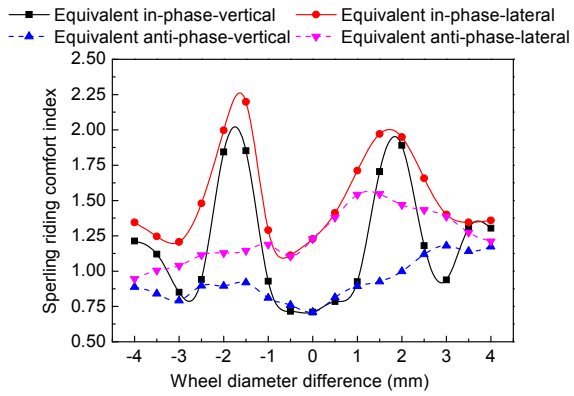

Fig. 18 Sperling indices under different wheel diameter differences

5.4 Wear index

The wear volume is dependent on the wheel-rail normal force and relative sliding. It can be assessed by the wear index that is related to creepage and creep force. It is combined with the frictional power in the separate direction and divided by the creep reference velocity. It is calculated by

$$w = |T_x v_x| + |T_y v_y| + |M_z \varphi_z|, \tag{7}$$

where w is the wear index; T_x and T_y are the creep forces in the longitudinal and lateral directions,

respectively; M_z refers to the creep torque; v_x and v_y are the longitudinal and lateral creepages, respectively; φ_z is the spin creepage.

As shown in Fig. 19a, when the small diameter wheel is at the stock rail side, with the large offset of wheelsets to the stock rail side, the flange contact increases the maximum wear index slightly with added wheel diameter difference amplitude. When the small diameter wheel is at the switch rail side, the wear index obtained under equivalent in-phase distribution of wheel diameter difference is higher than that obtained under equivalent anti-phase distribution. Focused on Figs. 19b and 19c, when the wheel diameter difference amplitude is below 2 mm, the distribution of the wear index in the longitudinal direction is similar to the change of lateral wheel-rail forces of flange contact. Their amplitudes increase quickly and the range of severe wear enlarges, causing the maximum value to reach 600.94 N. When the wheel diameter difference is over 2.5 mm, the stability of the train is fine under different wheel diameter difference distributions. However, the wear index quickly increases due to the continuous contact between the flange and working rail edge in the switch and crossing panel.

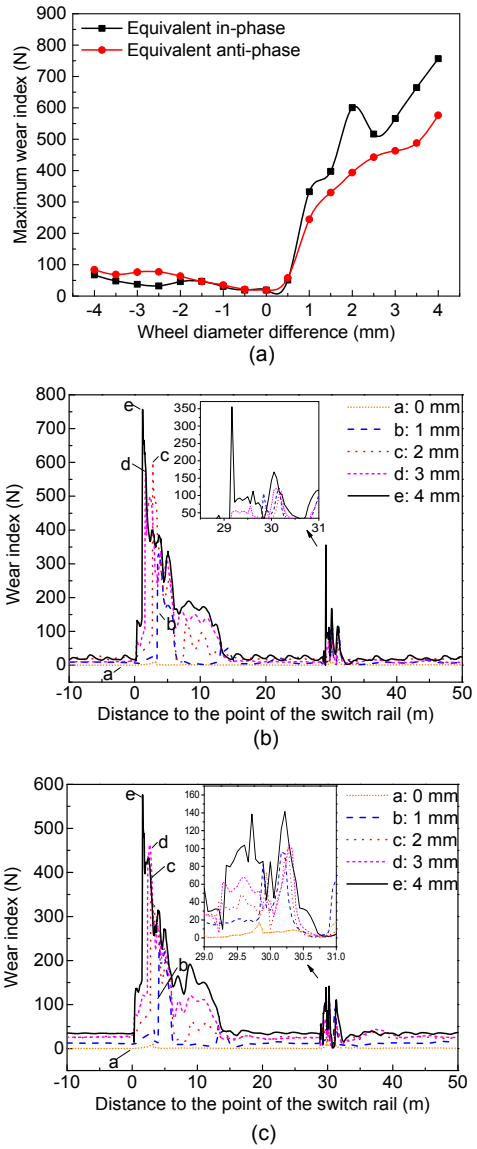

Fig. 19 Wear index of the guide wheelset: (a) comparison of the maximum wear index; (b) the wear index distribution of equivalent in-phase wheel diameter difference; (c) the wear index distribution of equivalent anti-phase wheel diameter difference

6 Conclusions

Taking wheel diameter difference in a variety of amplitudes and types and including equivalent in-phase and anti-phase distributions, the wheel-rail contact behaviour and the wheel-rail dynamic interaction in the turnout area have been investigated numerically. Results show that the wheel diameter difference has strongly affected their characteristics. The regulation is put forward and the following main conclusions are:

1. When the small diameter wheel is at the stock rail side, the wheel load transition position is advanced, and the vertical positions' variation of the wheel-rail contact points in the crossing panel increases by 16%. When the small diameter wheel is at the switch rail side, the wheel load transition position is moved backward. At the same time, the roll angle amplitude increases and the lateral wheel-rail contact point positions at the turnout zone greatly change.

2. The contact pressure in a turnout zone is affected by the wheel diameter difference changing the load transition position. When the small diameter wheel locates in the switch rail side, the added wheel diameter difference narrows the area of the contact patch on the switch rail and enlarges it on the curved stock rail. Peak values of contact pressure may be found on the switch rail surface. However, the added wheel diameter difference may optimize the contact position on the wheel and improve the conformal contact to decrease the contact stresses.

3. The equivalent in-phase wheel diameter difference has greatly increased the lateral wheel-rail force, which is mainly determined by the advanced flange contact with the switch rail and vehicle instability. As for the equivalent anti-phase wheel diameter difference, uneven distribution of vertical wheel-rail forces at both rail sides and increased lateral wheel-rail forces are found. To sum up, according to its amplitude, the effect of wheel diameter difference on wheel-turnout rail dynamic interaction can be divided into three: First, when the wheel diameter difference is within 0–1.5 mm, the flange contacts with the switch rail in advance, leading to quickly increased lateral wheel-rail force. Second, when it is within 1.5–2.5 mm, trains are subject to unstable running due to excitation of equivalent in-phase wheel diameter difference. The repeated motion of the wheelset near the equivalent pure rolling line leads the riding comfort index to reach a peak value rapidly. Third, when it is larger than 2.5 mm, the main wheel-rail contact point moves close to the flange and the wheelset is subject to repeated motion with low amplitude, leading to fine running stability and riding comfort but severe wear. It is recommended that for the allowed passing speed of 200 km/h in turnout, the wheel diameter difference should be controlled to within 2.5 mm to avoid severe wear, but limited to 2 mm for in-phase wheel diameter difference to ensure riding comfort.

The simulation allows for further development as the FASTSIM algorithm used in calculation model is quasi-static, which is generally accepted for excitation frequencies up to about 20 Hz. Therefore, the high frequency contribution for wheel-rail impact occurring at crossings is not included. In future work, analysis of the effect of wheel diameter difference combined with centrifugal force in the diverging route of turnouts can be carried out. Further given stochastic distribution of wheel diameter difference in variation of wheelsets, the evaluation of wheel diameter difference can get more comprehensive. Nevertheless, the presented regulation based on numerical simulation has provided theoretical guidance for wheel turning repair and analysis of the effect of profile wear on wheel-turnout rail interaction.

References

Bruni, S., Anastasopoulos, I., Alfi, S., *et al.*, 2009. Effects of train impacts on urban turnouts: modelling and validation through measurements. *Journal of Sound & Vibration*, **324**(3-5):666-689. http://dx.doi.org/10.1016/j.jsv.2009.02.016

Han, J., Zhao, G.T., Xiao, X.B., *et al*., 2015. Effect of softening of cement asphalt mortar on vehicle operation safety and track dynamics. *Journal of Zhejiang University-SCIENCE A (Applied Physics & Engineering)*, **16**(12): 976-986. http://dx.doi.org/10.1631/jzus.A1500080

Johansson, A., Pålsson, B., Ekh, M., *et al.*, 2011. Simulation of wheel–rail contact and damage in switches & crossings. *Wear*, **271**(1-2):472-481. http://dx.doi.org/10.1016/j.wear.2010.10.014

Kassa, E., Nielsen, J.C.O., 2009. Dynamic train–turnout interaction in an extended frequency range using a detailed model of track dynamics. *Journal of Sound & Vibration*, **320**(4-5):893-914. http://dx.doi.org/10.1016/j.jsv.2008.08.028

Kassa, E., Andersson, C., Nielsen, J.C.O., 2006. Simulation of dynamic interaction between train and railway turnout. *Vehicle System Dynamics*, **44**(3):247-258. http://dx.doi.org/10.1080/00423110500233487

Kuminek, T., Aniołek, K., Młyńczak, J., 2015. A numerical analysis of the contact stress distribution and physical modelling of abrasive wear in the tram wheel-frog system. *Wear*, **328-329**:177-185. http://dx.doi.org/10.1016/j.wear.2015.02.018

Lagos, R.F., Alonso, A., Vinolas, J., *et al.*, 2012. Rail vehicle passing through a turnout: analysis of different turnout designs and wheel profiles. *Proceedings of the Institution of Mechanical Engineers, Part F: Journal of Rail & Rapid Transit*, **226**(6):587-602. http://dx.doi.org/10.1177/0954409712445114

Ling, L., Xiao, X.B., Xiong, J.Y., *et al*., 2014. A 3D model for coupling dynamics analysis of high-speed train/track system. *Journal of Zhejiang University-SCIENCE A (Applied Physics & Engineering)*, **15**(12):964-983. http://dx.doi.org/10.1631/jzus.A1400192

Liu, X.F., He, Q.F., Liu, Y.J., 2008. Controlling rolling radii difference to eliminate flange bias-wear. The First International Symposium on Innovation & Sustainability of Modern Railway, p.528-533.

MOR (Ministry of Railways of the People's Republic of China), 2008. Vehicle Test Specification for High Speed Electric Multiple Units, Railway Transportation No. [2008] 28. MOR, China (in Chinese).

NBS (National Bureau of Standards), 1985. Railway Vehicles —Specification for Evaluation the Dynamic Performance and Accreditation Test, GB 5599-85. National Standards of People's Republic of China (in Chinese).

Ren, Z., 2013. Multi-point contact of the high-speed vehicle-turnout system dynamics. *Chinese Journal of Mechanical Engineering*, **26**(3):518-525. http://dx.doi.org/10.3901/CJME.2013.03.518

Ren, Z., Sun, S., Zhai, W., 2005. Study on lateral dynamic characteristics of vehicle/turnout system. *Vehicle System Dynamics*, **43**(4):285-303. http://dx.doi.org/10.1080/00423110500083262

Ren, Z., Iwnicki, S.D., Xie, G., 2011. A new method for determining wheel–rail multi-point contact. *Vehicle System Dynamics*, **49**(10):1533-1551. http://dx.doi.org/10.1080/00423114.2010.539237

Sawley, K., Urban, C., Walker, R., 2005. The effect of hollow-worn wheels on vehicle stability in straight track. *Wear*, **258**(7-8):1100-1108. http://dx.doi.org/10.1016/j.wear.2004.03.058

Wang, K.W., 1984. The track of wheel contact points and the calculation of wheel/rail geometric contact parameters. *Journal of Southwest Jiaotong University*, **1**:89-99 (in Chinese).

Wang, L., Wang, P., Quan, S.X., *et al.*, 2012. The effect of track alignment irregularity on wheel-rail contact geometry relationship in a turnout zone. *Journal of Modern Transportation*, **20**(3):148-152. http://dx.doi.org/10.1007/BF03325792

Wang, P., Xu, J.M., Xie, K.Z., *et al.*, 2016. Numerical simulation of rail profiles evolution in the switch panel of a railway turnout. *Wear*, **366-367**:105-115. http://dx.doi.org/10.1016/j.wear.2016.04.014

Xu, J.M., Wang, P., Wang, L., *et al.*, 2016. Effects of profile wear on wheel-rail contact conditions and dynamic interaction of vehicle and turnout. *Advances in Mechanical Engineering*, **8**(1):1-14. http://dx.doi.org/10.1177/1687814015623696

Zhang, B., Luo, Y.Y., 2015. Dynamic response of the track irregularity state in a subway turnout zone. Fifth International Conference on Transportation Engineering, p.1511-1517. http://dx.doi.org/10.1061/9780784479384.190

中文概要

题　目: 高速铁路轮径差激励下车轮-道岔动力响应数值研究

目　的: 车轮型面磨耗和加工误差导致轮对两侧车轮的轮径不同。本文旨在探讨不同幅值和分布形式的轮径差对道岔区轮轨接触几何、轮轨法向接触性能和车辆通过道岔动力响应的影响规律，提出保证车辆通过道岔时的安全性和舒适性的轮径差限值。

创新点: 通过数值仿真，分析轮径差对道岔区轮轨接触性能和轮轨动态相互作用的影响。

方　法: 1. 基于迹线法，揭示轮径差对道岔区轮轨接触几何的影响。2. 通过建立轮轨接触有限元计算模型，探讨轮径差对轮轨法向接触性能的影响。3. 通过建立车辆-道岔耦合动力学模型，综合考虑在不同幅值和分布形式的轮径差激励下，车辆通过道岔的轮轨动态相互作用、运行舒适性和磨耗指数评价指标，提出轮径差限值。

结　论: 1. 轮径差加剧了道岔区固有结构不平顺。2. 轮径差通过改变轮载过渡位置，对尖轨上的轮轨法向接触性能有较大影响。3. 可根据轮径差幅值将轮径差对道岔区轮轨动力响应的影响划分为三个区域：轮径差小于 1.5 mm 时，轮缘与尖轨提前接触使轮轨横向力快速增大；轮径差在 1.5~2.5 mm 时，等值同相轮径差使车辆通过道岔失稳；轮径差大于 2.5 mm 时，轮缘与尖轨的持续接触增强了车辆稳定性，但增加了轮轨磨耗。4. 建议将轮径差控制在 2.5 mm 以内，且应控制同相分布轮径差小于 2 mm。

关键词: 轮径差；道岔；轮轨接触行为；轮轨系统动力性能；高速铁路